

the Connectivity Map immediately suggests that sirolimus should be tested in a clinical trial of ALL patients with dexamethasone resistance. Sirolimus is already FDA approved as an immunosuppressant and is well tolerated in children, and the clinical prognosis of dexamethasone-resistant ALL is poor (37–40). This example demonstrates that the Connectivity Map is one approach to the rapid identification of new potential uses for existing drugs.

## Discussion

The value of a Connectivity Map depends on many open questions. How many distinct cellular pathways and states actually exist? How many cell types must be studied to provide sufficient diversity? How many perturbagens (small molecules, inhibitory RNAs, open reading frames) would need to be characterized to provide substantial coverage? How many concentrations, time points, and replicates would be required to provide reliable data? What analytical tools will be needed to interpret the data and determine precise estimates of statistical significance and false-positive rates? And, most important, what will be the biomedical value of the data? Only empirical evidence will resolve these issues.

Although only a first step, our results are encouraging. They show that genomic signatures can be used to recognize drugs with common mechanisms of action (HDAC inhibitors and estrogen receptor modulators), discover unknown mechanisms of actions (gedunin as an HSP90 inhibitor), and identify potential new therapeutics (the ability of sirolimus to overcome dexamethasone resistance in ALL). Our findings also reveal that signatures are often conserved across diverse cell types and settings (the signature of dexamethasone resistance was defined in bone-marrow samples but searched against profiles from the MCF7 breast cancer line). At the same time, the results demonstrate the limitations of using only a few cell lines (the signature of estradiol was not detected in cells that lack estrogen receptors) or only a few concentrations (chlorpromazine was not recognized as a phenothiazine at 1  $\mu$ M). It is also likely that our methodologies can still be refined. Indeed, alternative signature-based pattern-matching methods have been developed [e.g., (41)]. In addition, the interpretation of results depends on the ability to confidently call connections. More rigorous methods for the estimation of statistical significance are therefore probably also required, especially as the size of the database grows. But overall, the basic features of our approach appear to work well. We have, therefore, created a Web-based tool ([www.broad.mit.edu/cmap](http://www.broad.mit.edu/cmap)) to allow researchers to perform their own Connectivity Map analyses with user-defined signatures in real time.

On the basis of the results of this pilot study, we propose that a sensible next step would be the generation of an expanded Connectivity Map as a community resource project in the spirit of other genomic efforts. An initial goal might be to

profile all FDA-approved drugs and inhibitory RNAs targeting a large collection of genes in perhaps 10 diverse cell lines. Further goals would depend on the utility of the data. Ultimately, it will be interesting to explore whether it is possible to create a truly comprehensive catalog that begins to saturate all possible cellular states. In the meanwhile, even an incomplete Connectivity Map will likely accelerate progress in characterizing new chemical entities, finding new uses for existing drugs, and understanding the molecular mechanisms of disease.

## References and Notes

- J. L. DeRisi, V. R. Iyer, P. O. Brown, *Science* **278**, 680 (1997).
- J. Lamb *et al.*, *Cell* **114**, 323 (2003).
- T. R. Golub *et al.*, *Science* **286**, 531 (1999).
- C. M. Perou *et al.*, *Nature* **406**, 747 (2000).
- S. L. Pomeroy *et al.*, *Nature* **415**, 436 (2002).
- L. J. van 't Veer *et al.*, *Nature* **415**, 530 (2002).
- T. R. Hughes *et al.*, *Cell* **102**, 109 (2000).
- B. Ganter *et al.*, *J. Biotechnol.* **119**, 219 (2005).
- M. R. Fielden *et al.*, *Toxicol. Pathol.* **33**, 675 (2005).
- J. F. Waring *et al.*, *Toxicol. Appl. Pharmacol.* **175**, 28 (2001).
- M. Hollander, D. Wolfe, *Nonparametric Statistical Methods* (Wiley, New York, ed. 2, 1999), pp. 178–185.
- V. K. Mootha *et al.*, *Nat. Genet.* **34**, 267 (2003).
- A. Subramanian *et al.*, *Proc. Natl. Acad. Sci. U.S.A.* **102**, 15545 (2005).
- K. B. Glaser *et al.*, *Mol. Cancer Ther.* **2**, 151 (2003).
- J. Frasor *et al.*, *Cancer Res.* **64**, 1522 (2004).
- P. M. Martin, K. B. Horwitz, D. S. Ryan, W. L. McGuire, *Endocrinology* **103**, 1860 (1978).
- D. P. Edwards, W. L. McGuire, *Endocrinology* **107**, 884 (1980).
- A. E. Wakeling, M. Dukes, J. Bowler, *Cancer Res.* **51**, 3867 (1991).
- J. Y. Vanderhoek, M. B. Feinstein, *Mol. Pharmacol.* **16**, 171 (1979).
- B. L. Mylari, T. J. Carty, P. F. Moore, W. J. Zembrowski, *J. Med. Chem.* **33**, 2019 (1990).
- H. Hieronymus *et al.*, *Cancer Cell*, in press.
- S. A. Khalid, H. Duddeck, M. Gonzalez-Sierra, *J. Nat. Prod.* **52**, 922 (1989).
- M. E. Gorre, K. Ellwood-Yen, G. Chiosis, N. Rosen, C. L. Sawyers, *Blood* **100**, 3041 (2002).
- Q. Yao *et al.*, *Clin. Cancer Res.* **9**, 4483 (2003).
- I. P. Lopez *et al.*, *Obes. Res.* **11**, 188 (2003).
- B. M. Forman *et al.*, *Cell* **83**, 803 (1995).
- J. M. Lehmann *et al.*, *J. Biol. Chem.* **270**, 12953 (1995).
- J. M. Lehmann, J. M. Lenhard, B. B. Oliver, G. M. Ringold, S. A. Kliewer, *J. Biol. Chem.* **272**, 3406 (1997).
- T. M. Larsen, S. Toubro, A. Astrup, *Int. J. Obes.* **27**, 147 (2003).
- T. Kubota *et al.*, *Cancer Res.* **58**, 3344 (1998).
- R. Hata *et al.*, *Biochem. Biophys. Res. Commun.* **284**, 310 (2001).
- R. Ricciarelli *et al.*, *IUBMB Life* **56**, 349 (2004).
- B. J. Blanchard *et al.*, *Proc. Natl. Acad. Sci. U.S.A.* **101**, 14326 (2004).
- E. J. Hennessy, S. L. Buchwald, *J. Org. Chem.* **70**, 7371 (2005).
- W. J. Tissing, J. P. Meijerink, M. L. den Boer, R. Pieters, *Leukemia* **17**, 17 (2003).
- G. Wei *et al.*, *Cancer Cell*, in press.
- R. Pieters *et al.*, *Lancet* **338**, 399 (1991).
- T. Hongo, S. Yajima, M. Sakurai, Y. Horikoshi, R. Hanada, *Blood* **89**, 2959 (1997).
- G. J. Kaspers *et al.*, *Blood* **90**, 2723 (1997).
- G. J. Kaspers *et al.*, *Blood* **92**, 259 (1998).
- G. Natsoulis *et al.*, *Genome Res.* **15**, 724 (2005).
- We thank S. Schreiber, E. Scolnick, D. Altshuler, B. Wagner, B. Ebert, N. Tolliday, M. Brown, B. Wong, and members of the Broad Cancer and Chemical Biology Programs. This work was supported in part by grants from the National Cancer Institute, Howard Hughes Medical Institute, and The Paul G. Allen Family Foundation.

## Supporting Online Material

[www.sciencemag.org/cgi/content/full/313/5795/1929/DC1](http://www.sciencemag.org/cgi/content/full/313/5795/1929/DC1)

Materials and Methods

Figs. S1 to S5

Table S1

Signatures S1 to S11

Results S1 to S11

References

24 July 2006; accepted 6 September 2006

10.1126/science.1132939

# Structure of the 70S Ribosome Complexed with mRNA and tRNA

Maria Selmer,\* Christine M. Dunham,\* Frank V. Murphy IV, Albert Weixlbaumer, Sabine Petry, Ann C. Kelley, John R. Weir, V. Ramakrishnan†

The crystal structure of the bacterial 70S ribosome refined to 2.8 angstrom resolution reveals atomic details of its interactions with messenger RNA (mRNA) and transfer RNA (tRNA). A metal ion stabilizes a kink in the mRNA that demarcates the boundary between A and P sites, which is potentially important to prevent slippage of mRNA. Metal ions also stabilize the intersubunit interface. The interactions of E-site tRNA with the 50S subunit have both similarities and differences compared to those in the archaeal ribosome. The structure also rationalizes much biochemical and genetic data on translation.

A major breakthrough for our mechanistic understanding of translation was achieved some years ago when high-resolution structures of the 50S and 30S ribosomal subunits were solved (1, 2). Progress has also been made in obtaining structural data on the whole ribosome. The subunit structures were used to facilitate interpretation of maps at 5.5 Å resolution of the whole 70S ribosome complexed

with mRNA and tRNA (3). More recently, the structure of the *Escherichia coli* ribosome was solved at 3.5 Å resolution (4). At the same

MRC Laboratory of Molecular Biology, Hills Road, Cambridge CB2 2QH, UK.

\*These authors contributed equally to this work.

†To whom correspondence should be addressed. E-mail: ramak@mrc-lmb.cam.ac.uk

time, electron cryomicroscopy (cryo-EM) studies have yielded increasingly detailed structures of various functional states of the ribosome (5).

Important as these results are, current structural data on whole ribosomes have limitations. At resolutions lower than 3.5 to 4 Å, it is possible to model known structures into maps but difficult to interpret previously unknown regions in molecular terms. For example, in the 5.5 Å crystal structure of the 70S ribosome, an attempt was made to interpret the L1 and L7/L12 stalks, which consist of both proteins and RNA (3). These interpretations were at variance with high-resolution structures of the components determined later (6, 7). Typical cryo-EM maps of the ribosome have even lower resolution and thus suffer the same limitations. The 3.5 Å resolution crystal structure of the empty *E. coli* ribosome (4) allowed many molecular details to be seen directly. However, this structure lacks direct information about the interactions of the ribosome with its mRNA and tRNA ligands.

We report here the structure of a pretranslocation state of the *Thermus thermophilus* ribosome at 2.8 Å resolution, which has allowed us to build an accurate model that reveals the structures of tRNA and mRNA in situ and the molecular details of their interaction with the ribosome.

#### Crystallization and structure determination.

A pretranslocation complex of the ribosome was formed by complexing it with mRNA, deacylated initiator tRNA<sup>fMet</sup> in the P site, and aminoacyl tRNA<sup>Phe</sup> in the A site (8). The antibiotic paromomycin, which is known both to increase the affinity of A-site tRNA and to inhibit translocation, was also included.

An extensive search for well-diffracting crystals led to a new crystal form grown in a mixture of 3.5 to 4.5% (w/v) PEG20K and 3.5 to 4.5% (v/v) PEG550MME at pH = 7. The crystals

were in space group P2<sub>1</sub>2<sub>1</sub>2<sub>1</sub> (cell dimensions of  $a = 214$  Å,  $b = 454$  Å,  $c = 630$  Å, and  $\alpha = \beta = \gamma = 90^\circ$ ) and contained two copies of the 70S ribosome in the asymmetric unit. A molecular replacement solution was found by using a model of the *T. thermophilus* ribosome (9) that was derived from atomic models of the 30S (2) and 50S (1, 10) ribosomal subunits. All ligands were removed from the search model before its use. This solution was used as a starting point to build the structure and refine it to 2.8 Å resolution. The mRNA, tRNA, and antibiotic ligands were only included in the final rounds of refinement, so that they could be built into unbiased difference Fourier maps (8). A summary of crystallographic data and refinement statistics is given (table S1).

After refinement, the tRNA and mRNA ligands, as well as differences from the input model, could clearly be seen in difference Fourier maps (Fig. 1). It was easily possible to distinguish between purines and pyrimidines, and well-ordered side chains of proteins were clearly visible. It was also possible to see a large number of metal ions.

The current structure consists of nearly the entire 70S ribosome with its tRNA and mRNA ligands (fig. S1). The L7/L12 stalk, along with its base consisting of the L10, L11, and L6 regions as well as the elbow and acceptor arm of A-site tRNA, was poorly ordered or disordered. The E site was occupied with a noncognate tRNA.

In the following description of the structure, we focus mainly on those details that have not been seen directly in previous work. These include details of the interactions of tRNA and mRNA with the ribosome and the participation of proteins and metal ions, especially in intersubunit bridges. For the sake of conciseness, we refer to the ribosomal subunits as 30S and 50S, and to the whole ribosome as 70S.

**Overall structure.** The two molecules in the asymmetric unit are nearly identical, in contrast to the two ribosomes in the asymmetric unit of the *E. coli* 70S crystals (4). Surprisingly, even mobile regions such as the L1 stalk of the 50S are in similar conformations. Thus, binding of mRNA and tRNA confers conformational homogeneity to the ribosome.

The structure of the 50S is very similar to that of both 50S molecules in the asymmetric unit of the *E. coli* 70S crystals (4). The only significant difference is that the regions surrounding the E site are further apart in the empty ribosome but move toward each other to bind E-site tRNA (fig. S2). The most notable movement is that of the L1 stalk. Differences in the L1 stalk conformation have also been observed between empty 50S and previous 70S structures containing E-site tRNA (1, 3, 10).

In contrast, the 30S subunit of the 70S complex reported here is more similar to the closed 30S form described previously, as a consequence of A-site tRNA binding (11), than to either of the two 30S molecules of the empty *E. coli* ribosome (4), which are both more open to varying degrees (fig. S3). A comparison of the rmsd and median distance of equivalent phosphorus atoms for the subunits from various 70S structures is shown in table S2.

An *E. coli* numbering for *Thermus* ribosomal RNA (rRNA) based on structural alignment with the *E. coli* ribosome (4) is used throughout. We also used the standard Brimacombe helix numbering for rRNA, with a lowercase h prefix for 16S RNA and an uppercase H for 23S RNA.

**Interactions with tRNA and mRNA.** In the hybrid states model, tRNAs move first relative to the 50S subunit and then with respect to the 30S subunit during translocation (12). Thus

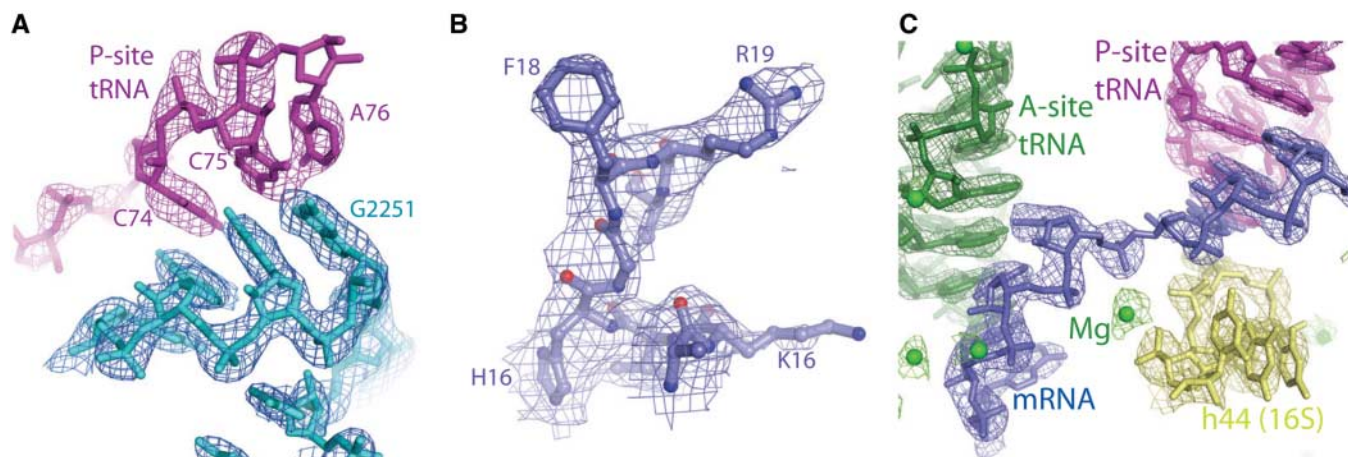


**Fig. 1.** Representative electron density in the 70S structure. (A)  $F_o - F_c$  map showing unbiased density of the acceptor end of P-site tRNA (not included in the refinement), with refined  $3F_o - 2F_c$  density for 23S RNA. Base pairs between C74 and C75 with G2252 and G2251 of 23S RNA are clearly visible. (B) Simulated annealing omit map of the large subunit protein L34 showing the visibility of well-ordered side chains. (C) A Mg

ion shown in unbiased difference Fourier maps that is coordinated to the nonbridging phosphate oxygens at the 45° mRNA kink between the A and P site as well as the nonbridging phosphate oxygens of nucleotides 1400 and 1401 of h44 of 16S RNA. All RNA is shown in final  $3F_o - 2F_c$  density. The Mg ions are shown in green. This and all other figures were made with Pymol (47).

during the intermediate step, a tRNA could be in the P site of the 30S and the E site of the 50S, or in the A site of the 30S and the P site of the 50S (designated as P/E or A/P states). In the structure described here, the tRNAs were in the classical P/P or E/E states, as would be expected for a state before translocation.

**The A site.** The A site of the ribosome is where codon-anticodon interactions are monitored in the decoding site of the 30S subunit and where the new amino acid at the 3' end of tRNA is made available for peptide bond formation in the peptidyl transferase center (PTC) of the 50S subunit. The anticodon stem loop (ASL), comprising nucleotides 26 to 44, was clearly visible in the decoding center of the 30S subunit, with an orientation that corresponds to the accommodated form in which the acceptor arm is in the PTC. Surprisingly, although full-length aminoacylated tRNA<sup>Phe</sup> was used in crystallization and its binding was stabilized by paromomycin, the rest of the tRNA was not visible in the density. We believe that this is due to deacylation of tRNA<sup>Phe</sup> during crystallization, which results in a reduction of affinity for the PTC and a disorder of the acceptor arm. Deacylation also allows the tRNA to bind to the E site.

The ASL of the tRNA, the A-site codon, as well as the 16S RNA nucleotides G530, C1054, A1492, and A1493, superimpose perfectly with the structure of ASL<sup>Phe</sup> in the 30S subunit (13), confirming the interactions of A1492, A1493, and G530 with the minor groove of the first two codon-anticodon base pairs and the packing of C1054 against the wobble base pair. This also validates studies on decoding using the 30S subunit with an mRNA interrupted between the A and P sites (11, 13). There is only one direct contact of the ASL with 23S RNA, where A1913 in intersubunit bridge B2a forms a hydrogen bond to the 2'-OH of ribose 37.

**The P site.** Except during initiation, the tRNA has already been selected by the time it is translocated to the P site, and codon-anticodon interaction is not monitored. Instead, the P site has evolved mainly to hold the tRNA tightly in position to maintain the reading frame and for peptidyl transfer. The entire P-site tRNA<sup>fMet</sup> was visible in an unbiased difference Fourier map, a portion of which is shown (Fig. 1A). As seen in the 5.5 Å structure (3), the P-site tRNA makes extensive contacts with both ribosomal subunits, with 2481 Å<sup>2</sup> or 19% of its surface area buried in interactions with the ribosome or mRNA (Fig. 2A). The distinguishing features of initiator tRNA were clearly seen. These include the absence of a Watson-Crick base pair at C1-A72, a purine-pyrimidine base pair, 11-24, and three consecutive GC base pairs in the anticodon stem (14, 15).

**Interactions of P-site tRNA with mRNA and the 30S subunit.** The backbone of the mRNA codon in the P site interacts with C1402, C1403, and U1498 of 16S RNA. In addition, we saw a metal ion that bridged C1401 and G1402 to the codon. G1401 was shown in modification interference experiments to be important for codon-dependent P-site tRNA binding (16). The wobble base pair is held in place by stacking interactions from two sides; C1400 stacks with the base pair and G966 against the ribose of C34 (Fig. 2B). Recent mutagenesis on the P site showed that mutation of C1400 to a purine reduces translation at least 12-fold (17), presumably because a purine would clash with G966 in the current structure and the distortion required to accommodate it would lower the affinity of P-site tRNA.

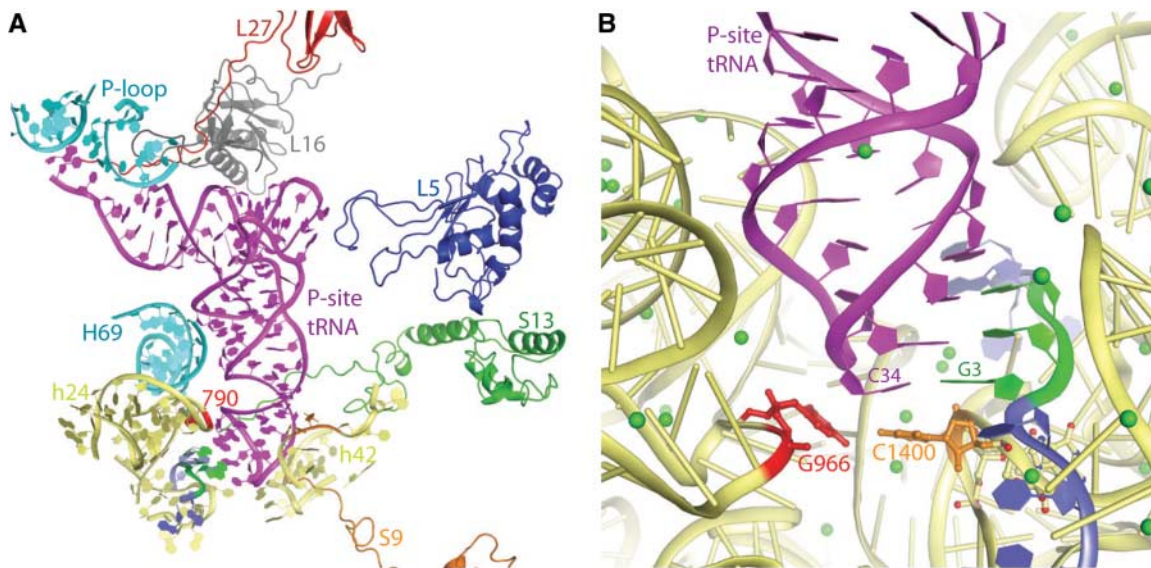
Interestingly, A1339 was identified as a critical nucleotide in mutational studies of the 30S P site (17). A1339 and G1338 of 16S RNA form type I and type II A-minor interactions (18) with the GC base pairs 30-40 and 29-41 of P-site

tRNA (Fig. 3A). These are two of the three consecutive GC pairs in the anticodon stem loop that are characteristic of initiator tRNA and that have been implicated as being important for initiation. Because these interactions are stronger with GC base pairs than AU (19), this suggests an explanation for additional stabilization of initiator tRNA compared with other tRNAs. The importance of these minor groove interactions in discrimination of initiator tRNA has been established in recent mutagenesis studies (20). However, as the authors point out, it is not entirely clear why three rather than just one or two GC pairs are required; other factors are likely to be important in initiator tRNA selection. Interestingly, A1339 makes a suboptimal A-minor interaction, with the distance between the N1 of A1339 and the 2'-OH of G29 too long for a hydrogen bond (4 Å; marked with an "x" in Fig. 3A). It is possible that during initiation, small conformational changes in the head induced by the binding of initiation factor IF3 bring the head into an optimal orientation to inspect the initiator tRNA.

A1339 and G1338 in the head of the 30S interacts with the ASL of P-site tRNA on one side, while nucleotide 790 at the tip of the 30S platform contacts the ASL on the other side, thus preventing its movement into the E site (Fig. 3B). During translocation of tRNA from the P to the E site, these two elements would have to move apart, presumably by a movement of the head (4, 21). Thus, G1338 and A1339 may not only confer additional stability to initiator tRNAs but may also act as a switch during both initiation and translocation.

Two protein tails from the 30S extend into the P site (Fig. 2A) (22). Lys<sup>127</sup> of S9 interacts with the phosphate oxygens of P-site tRNA positions 33 and 34, and the backbone of S13 at residue 118 comes close to the phosphate oxygens of P-site tRNA position 29.

**Fig. 2.** P-site tRNA interactions with the ribosome. (A) Overview of both RNA and protein interactions with P-site tRNA. P-site tRNA interacts with many ribosomal protein tails such as L27, L16, L5, S13, and S9 and 16S and 23S RNA. 16S RNA bases 790 and 1338 and 1339 interact with the anticodon stem, thereby acting as a gate between the P and the E site. (B) Interaction of the anticodon loop with mRNA and the 30S subunit. The wobble base pair (C34-G3) is held in place from two sides by 16S RNA base C1400 that stacks on the wobble base pair and by 16S RNA base G966 that stacks against the ribose of C34.



In the structure of the 30S, the spur of a symmetry-related molecule interacted with the 3' end of the 16S RNA, mimicking a P-site codon-anticodon interaction (22). Because this interaction formed noncanonical pyrimidine-pyrimidine base pairs at all three positions, it was not clear how accurately the structure represented the details of true tRNA-codon interactions. The present structure shows that despite the noncanonical base pairs, the spur in the 30S is indeed an excellent mimic of the ASL part of the tRNA. The main differences are that G966 packs optimally against the ribose of anticodon nucleotide 34 and that the upper part of the ASL in the spur of the 30S was displaced by 4 Å relative to the P-site tRNA in the 70S structure.

The P-site tRNA was distorted relative to the isolated crystal structure of yeast tRNA<sup>Phe</sup> (fig. S4) (23, 24). A deformation of the anticodon stem was caused by opposing interactions with the head of the 30S subunit and H69 of the 50S subunit, resulting in an opening up of the major groove around the 26:44 base pair. Interestingly, this means that if constraints on the tRNA were released in the 50S, e.g., after peptidyl transfer, relaxation of the deformation would have the effect of driving the tRNA toward the E site (fig. S4).

**Interactions at the PTC.** The acceptor end of P-site tRNA interacts with the PTC in the 50S subunit in a manner similar to that observed for oligonucleotide mimics of tRNA soaked into the *Haloarcula* 50S subunit [e.g., (25, 26)], in contrast to the suggestion that the orientation of tRNA in the PTC is determined by remote interactions (27). Bases C74 and C75 form Watson-Crick base pairs with G2252 and G2251, while the terminal A76 stacks with 75 and 74 and forms an A-minor interaction with

the A2450-C2063 base pair (Fig. 4). The 2'-OH of A76 is in hydrogen-bonding distance of both the N3 and 2'-OH of A2451, showing its importance in stabilizing the conformation of P-site tRNA. The 2'-OH of A76 and nucleotide A2451 are known to be important for peptidyl transferase activity and for substrate stabilization (28, 29).

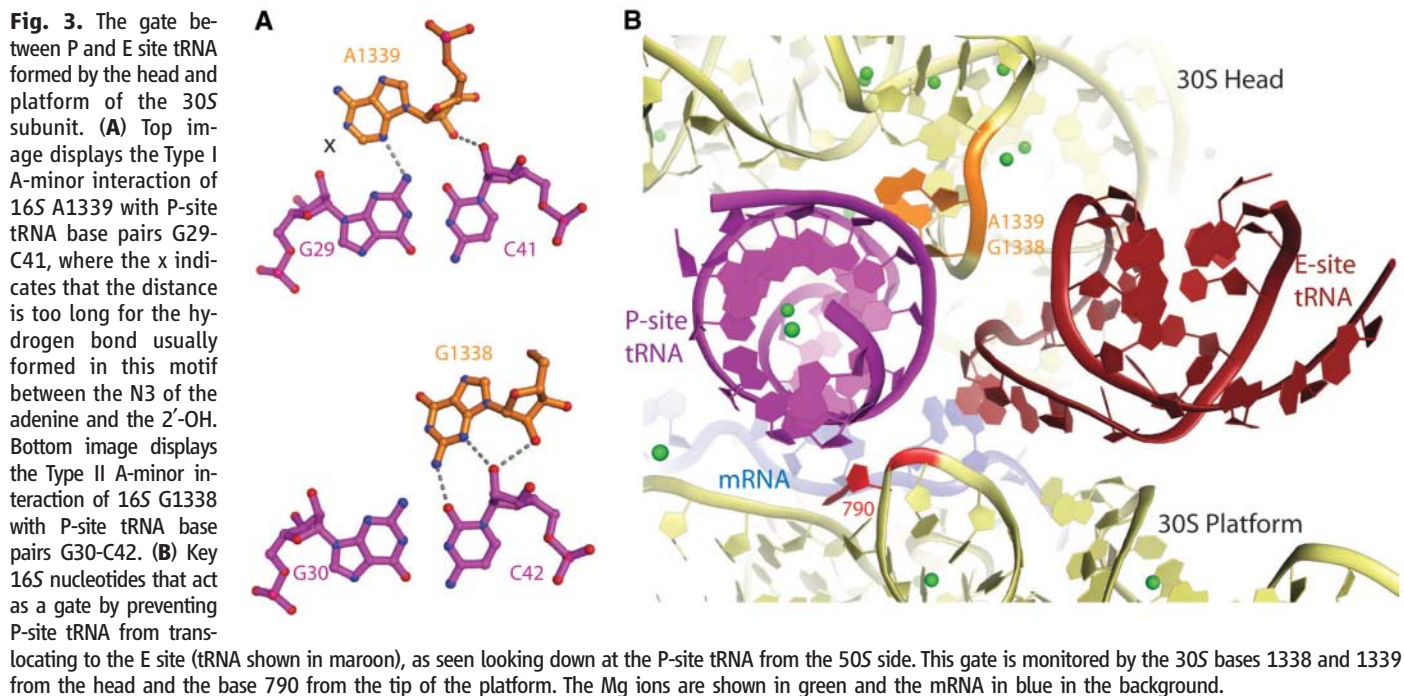
The PTC itself was in a very similar conformation to those reported in studies of the *Haloarcula* 50S with various ligands as well as to the PTC of the *Deinococcus radiodurans* 50S subunit (10). The A and P loops superimposed closely, with the P loop accommodating an extra nucleotide in the *Haloarcula* structure while closely maintaining the positions of the other bases. Nucleotides known to be mobile in the 50S subunit (28, 29), such as A2062 at the entrance to the nascent peptide channel and A2602, which lies between the A and P sites, also appeared to be mobile in our structure, because they had significantly weaker density. The conformation of the PTC was also similar to that of the empty *E. coli* 70S structure (4). Although concerted differences in the conformation of the PTC between the *E. coli* and *Haloarcula* 50S structures were reported (4), those differences are small and comparable in magnitude to the difference between the current structure and the *E. coli* structure or to differences between apo- and ligand-bound *Haloarcula* structures (rmsd ~ 0.7 Å).

In *E. coli*, the N-terminal tail of L27 can be cross-linked to A76 of P-site tRNA (30), and deletion of as few as the first three residues can significantly reduce peptidyl transferase activity (31). These observations suggest that the N terminus of L27 is close to or at the PTC. In the 70S structure, L27 has the fold of the crystal

structure of the isolated protein (32) rather than that reported in the *Deinococcus* 50S subunit structure (10). It is well defined from residue 10 onward, but very weak density is also visible for residues 1 to 9. The density is consistent with a position of the N terminus close enough to interact with A76 of P-site tRNA, where it could additionally stabilize the P-site substrate and thereby enhance peptidyl transferase activity. This is in contrast to the *Haloarcula* 50S structure, in which Asp<sup>111</sup> of L10e, adjacent to a disordered loop, is 11.5 Å away (26). We also find that the closest ordered metal ion is 8.5 Å away from the 3'-OH of A76, in agreement with studies on the *Haloarcula* 50S structure reporting the absence of metal ions in the immediate vicinity of the PTC (26).

Apart from the ASL and CCA ends, other parts of the P-site tRNA makes extensive interactions with the 50S subunit (Fig. 2A). As seen earlier at 5.5 Å (3), H69 of 23S RNA makes direct minor groove interactions with the D helix (nucleotides 11 and 12) and also with the adjacent nucleotides 24 and 25 in the anticodon stem. At the elbow, protein L5 forms two hydrogen bonds with C56, and L16 is close to G53 but too far to make an interaction in the current structure. Also, we saw five Mg ions coordinated within the tRNA and a sixth bringing together the nonbridging phosphate oxygens of tRNA nucleotides 75 and 76 and 23S RNA nucleotide 2602.

**The E site.** During translation, the ribosomal E site is occupied by deacylated tRNA that has been translocated from the P site. The nature and role of the E site remains controversial. E-site tRNA was postulated to bind both 30S and 50S subunits and to make interactions with the codon of mRNA (33). However, footprinting and other



biochemical data questioned the existence of an E site on the 30S (34, 35). The 5.5 Å structure of the *Thermus* ribosome unambiguously established the presence of an E site in both the 30S and 50S subunits (3). However, at that resolution it was unclear to what extent codon-anticodon base pairing occurred.

We saw density for E-site tRNA, and the absence of the insertion at nucleotide 17 that was present in initiator tRNA<sup>fMet</sup> as well as other features identify it as deacylated tRNA<sup>Phe</sup>. Both the anticodon and CCA ends of tRNA are well defined, whereas some regions around the elbow region are poorly ordered.

**The 30S E site.** We did not observe any codon-anticodon interactions in the E site. In fact, A35, the middle anticodon base, was closer to G693 of 16S RNA than to the E-site codon. The tRNA here is noncognate, but it would not be possible to make codon-anticodon base pairs even with a cognate codon unless the mRNA or tRNA were to move significantly relative to their present locations (Fig. 5A). Whereas A and P site tRNAs made extensive interactions with 16S RNA, the 30S E site is primarily made of proteins S7 and S11, as seen earlier (3, 22), explaining the absence of footprints to 16S RNA (34).

**The 50S E site.** In the 50S, the acceptor end of E-site tRNA interacts with residues at the base of H82, whereas bases at the ends of the T and D loops interact with the L1 stalk, thus stabilizing the stalk in a closed conformation. A number of tRNA mutations and modifications that affect translocation are thought to have altered interactions with the 50S E site, presumably during the formation of the P/E hybrid state. The interactions of tRNA with the 50S E site were seen in sufficient detail to analyze these data (Fig. 5B).

The base and 2'-OH of A76 have been shown to dramatically affect E-site tRNA binding and translocation (36, 37). The base of A76 intercalates between G2421 and A2422 of 23S RNA and makes hydrogen bonds with the universally conserved C2394, as seen recently in the E site of the *Haloarcula* 50S subunit, by using a minihelix representing the acceptor arm of tRNA (38). The 3'-OH of A76 is surrounded by 23S RNA elements, and the site could not accommodate an amino acid on the tRNA, explaining the requirement for deacylated tRNA.

However, the interactions of E-site tRNA in the bacterial 70S structure also show striking differences from those in the archaeal *Haloarcula* 50S subunit. The orientations of the acceptor arms were different, possibly because the minihelix used in the *Haloarcula* structure lacked the D and T loops that make interactions with the L1 stalk. Moreover, we find that C75 stacks directly on C74, whereas in the archeal structure the base of C75 was splayed out from the tRNA in the opposite direction from A76, where it was stabilized by interactions with L44e (38). This protein is not present in bacterial ribosomes, and in any case such a conformation would be precluded by clashes with U2431 and A2432 and by the presence of protein L28 (previously identified as L31).

**Fig. 4.** P-site tRNA interactions at the PTC. The CCA end of P-site tRNA in the PTC interacts with conserved 23S RNA bases A2451 and the P loop. Specifically A76 is stacked with both C75 and C74, and its 2'-OH interacts with both the N3 and 2'-OH of A2451. C74 and C75 form Watson-Crick base pairs with P-loop bases G2252 and G2251. The N-terminal tail of L27 (blue) is shown in the background and is known to be close to A76 from biochemical studies.

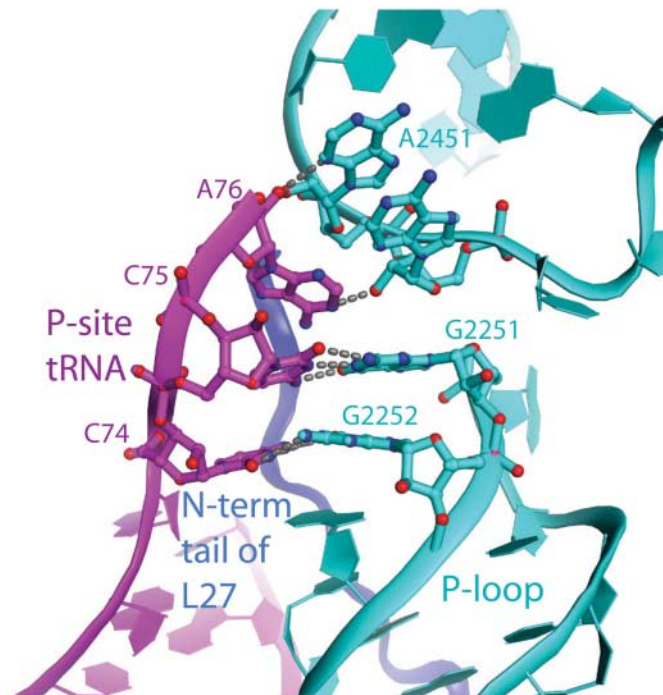
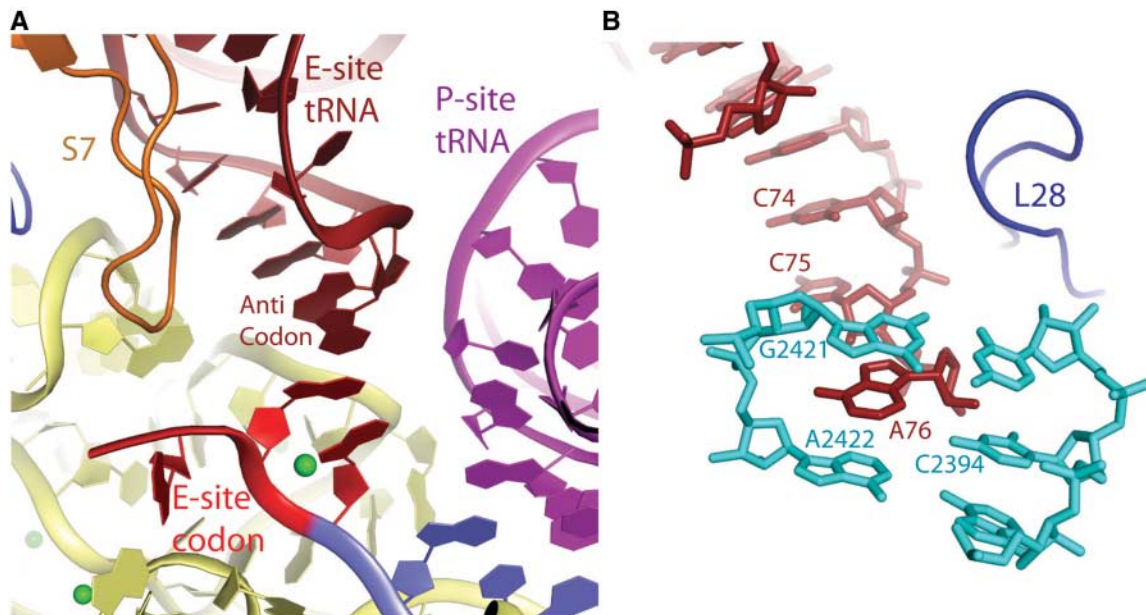


**Fig. 5.** E-site interactions in the 70S. (A) The anticodon of a noncognate E-site tRNA does not interact with the E-site codon of mRNA. Mg ions are shown in green. (B) A76 at the acceptor end of E-site tRNA intercalates between bases G2421 and A2422 of 23S RNA and interacts with the conserved base C2394. C75 is stacked on C74 and is in a markedly different conformation from that previously observed in an archaeal 50S subunit (38).



The common mode of binding of A76 suggests that the existence of the E site predates the divergence of bacteria from archaea. However, differences in the conformation of C75 and the identities of the proteins present suggest that the E site has subsequently evolved differently in bacteria and other kingdoms.

**General features of mRNA.** The sharp kink between the A- and P-site codons (3) clearly delineates the border between these two sites and presumably is important for defining the reading frame and preventing slippage of the mRNA. In the 70S structure, this kink is stabilized by a Mg ion, which makes interactions with the phosphate oxygens of the third P-site nucleotide and the first A-site nucleotide, allowing them to come closer together (Fig. 1C). Interactions of the Mg ion with phosphate oxygens of nucleotides 1401 and 1402 of 16S RNA further fix the frame of mRNA with respect to the 30S subunit.

Apart from the codons at the tRNA binding sites, we saw two additional nucleotides beyond the E site. The rest of the mRNA appeared disordered, just as in the 5.5 Å 70S crystal structure (3), although Yusupova *et al.* could see its extended path, including the Shine-Dalgarno interaction at the 5' end, by using a low resolution difference Fourier map between ribosomes containing and lacking mRNA (39).

**Overview of proteins.** Whereas the 30S proteins were little changed from the 30S structure of the same species (2), all of the 50S proteins in the structure had to be rebuilt, some of them *ab initio* (8) (table S3). We report here some significant differences from previous work.

A region of the 50S subunit was originally interpreted as corresponding to protein L31 (10), and this interpretation was subsequently propagated into low-resolution structures of the 70S ribosome as well as that of the higher-resolution *E. coli* ribosome structure (4). However, this region of the electron density showed an additional  $\alpha$  helix that could be accounted for by the L31 sequence. Moreover, it is a region where cross-links have been observed to ribosomal protein L28 (40), whereas no biochemical data connected it to L31. We could satisfactorily build the L28 sequence into the electron density.

At the same time, unexplained density was found for a protein adjacent to protein L5 (fig. S5). We suggest that this is protein L31 on the basis of reports that it formed a cross-linked dimer with L5 (41). This location of L31 would also be consistent with the ease with which it dissociates from the ribosome (42). Helical density from L31 packs against an  $\alpha$  helix of L5 and the intersubunit surface  $\alpha$  helix of S13.

We saw no evidence for L36, although the structure of this protein from *Thermus* has been solved in isolation (43). Interestingly, the pocket where L36 was seen in the *Deinococcus* 50S (10) was also empty in the *Haloarcula* 50S (1). It is possible that the protein was lost

during purification, but, given the nature of the pocket and the highly charged nature of L36, we consider this unlikely. An alternative hypothesis is that the protein is not a true ribosomal protein, but this idea would be difficult to reconcile with its presence in the *Deinococcus* 50S structure (10).

**Intersubunit bridges.** During translation, ribosomal subunits need to associate during initiation and dissociate during recycling after termination. However, they also need to move relative to each other, especially during translocation (21). Because translation is a highly specific and intricate process, the association of ribosomal subunits, as well as the changes in their interaction during relative movement, must be both highly specific as well as dynamic. It has also been known for almost 50 years that ribosomal subunits from all species studied can reversibly associate and dissociate *in vitro* as a function of Mg concentration, suggesting the universal importance of divalent ions in intersubunit contacts (44).

The interactions between subunits occurs through a number of bridges, first seen and named as B1 to B6 in cryo-EM maps of the ribosome (45). In particular, the long penultimate h44 of 16S RNA extended from the interdomain junction of the 30S to the bottom of the subunit and made a number of intersubunit contacts (Fig. 6A). These bridges are essential for subunit association, but some of them also need to be formed and broken during the translation process. The 5.5 Å structure of the ribosome described the molecular components that make up the bridges, subdividing the classification further (3). The 3.5 Å structure of the *E. coli* ribosome described many of these interactions in greater detail, especially between components of rRNA. The various bridges differ in character, probably reflecting their nature as static or dynamic contacts. We saw not only the RNA elements but also the side chains of proteins, as well as ions that are involved in the formation of bridges (table S4). Apart from being essential to our understanding of intersubunit interactions, these details help rationalize recent biochemical and genetic data as well as the role of metal ions in subunit association. We describe some examples of bridges: an induced conformational change in a bridge as a result of tRNA binding, a bridge that is entirely mediated by a metal ion, and a bridge in which both metal ions and protein side chains contribute to bridge formation.

In bridge B2a, H69 of 23S RNA (3, 4) extends across the interface to interact with h44 of 16S RNA. The loop of H69 was disordered in the *Haloarcula* 50S (1) and formed a compact structure in *Deinococcus* 50S (10). However, comparison of our structure to the *E. coli* 70S structure shows that A1913 of H69 flips to insert into a tight pocket formed by the backbone of h44 and A-site tRNA, forming a hydrogen bond between its N1 to the 2'-OH of

A37 of A-site tRNA (Fig. 6B). The base is then oriented toward the bases of A1492 and A1493 that flip out during decoding to interact with tRNA and mRNA (13). A Mg ion bridges the ribose O4' of A1913 of H69 with a phosphate oxygen of position 38 of A-site tRNA, and a second Mg ion bridges the ribose 2'-OH with the nonbridging phosphate oxygens of 16S 1493 and 1494. The result of this rather tight interaction in combination with the h44 movement to monitor decoding is that the entire H69 is shifted slightly toward the 30S subunit relative to the empty *E. coli* structure. This conformational change may offer one route for signaling correct 30S decoding to the 50S guanosine triphosphatase center before tRNA accommodation.

B2c is a purely Mg-mediated bridge in which ordered metal ions mediate interactions between the backbones of h24 and h27 of 16S RNA and H67 of 23S RNA (Fig. 6C and table S4). The structure rationalizes the observation that phosphothiorate substitution at C770 in h24 of 16S RNA is not tolerated, presumably because it would inhibit Mg-dependent subunit association via nonbridging phosphate oxygens (46). In addition to B2c where they are crucial, metal ions also appear to confer additional stability to B5, B6, and B8 (table S4).

Proteins in the bridges interact with RNA, other proteins, and metal ions. The direct interactions of proteins to RNA in bridges seem to be entirely to the backbone rather than to specific bases. Such interactions may be characteristic of dynamic elements that have to make different contacts in different states of the ribosome. In B5, the only direct interaction between L14 and 16S RNA is between Arg<sup>49</sup> of L14 and a nonbridging phosphate oxygen of nucleotide 1423 of 16S (Fig. 6D). Interestingly, a Mg ion is coordinated to the nonbridging phosphate oxygens of 1421 of h44, 1950 and 1951 of H71, and Glu<sup>54</sup> of L14 (Fig. 6D). Additionally, L14 and L19 also interacted with two ordered Mg ions in B8 (Fig. 6E).

In B6, the minor grooves of h44 and H62 approached each other but left a 6 Å gap as seen in the *E. coli* structure, where it was suggested that there might be a monolayer of water molecules (4). We observed one ordered solvent molecule that is coordinated by the backbone of nucleotides 1703 and 1704 of H62 and 1429 and 1430 of h44.

In the *Thermus* 70S structure, there appears to be an additional bridge (not present in *E. coli*) involving an interaction of G1442a at the bottom of h44 and a nonbridging phosphate oxygen of 23S G2864 of 23S RNA that is mediated by an extended loop of L19. This contact might lend some additional stability to the *Thermus* ribosome and is the only example of a protein interaction with an RNA base rather than its backbone.

**Conclusions.** The structure of the 70S ribosome describes the detailed interactions of the

mRNA and tRNA substrates with the ribosome, the interactions between the ribosomal subunits, and the role of metal ions in the structure. The interactions of A-site tRNA in the decoding center and P-site tRNA at the PTC were in good agreement with work done on the 30S and 50S subunits using oligonucleotide mimics of tRNA. We saw no codon-anticodon interactions with the noncognate tRNA in the E site. The interactions of E-site tRNA with the 50S subunit showed both similarities and differ-

ences with the previously studied *Haloarcula* E site. The involvement of magnesium ions has long known to be crucial for several aspects of translation, such as subunit association and codon-dependent tRNA binding. We saw metal ions in key positions of critical areas, such the interface between subunits and between the ribosome and tRNA and mRNA. In particular, a magnesium ion stabilized a kink in mRNA at the boundary between the A- and P-site codons, which is of potential importance in preventing

slippage during translation. The structure helps to rationalize much detailed biochemical, mutational, genetic, and conservation data and should be useful for the design of future experiments. Moreover, because the A and P sites of the structure are relatively protected from crystal contacts, it is hoped that this crystal form will pave the way for high-resolution structures of functional complexes involving other substrates as well as 50S antibiotics that require an occupied P-site substrate.

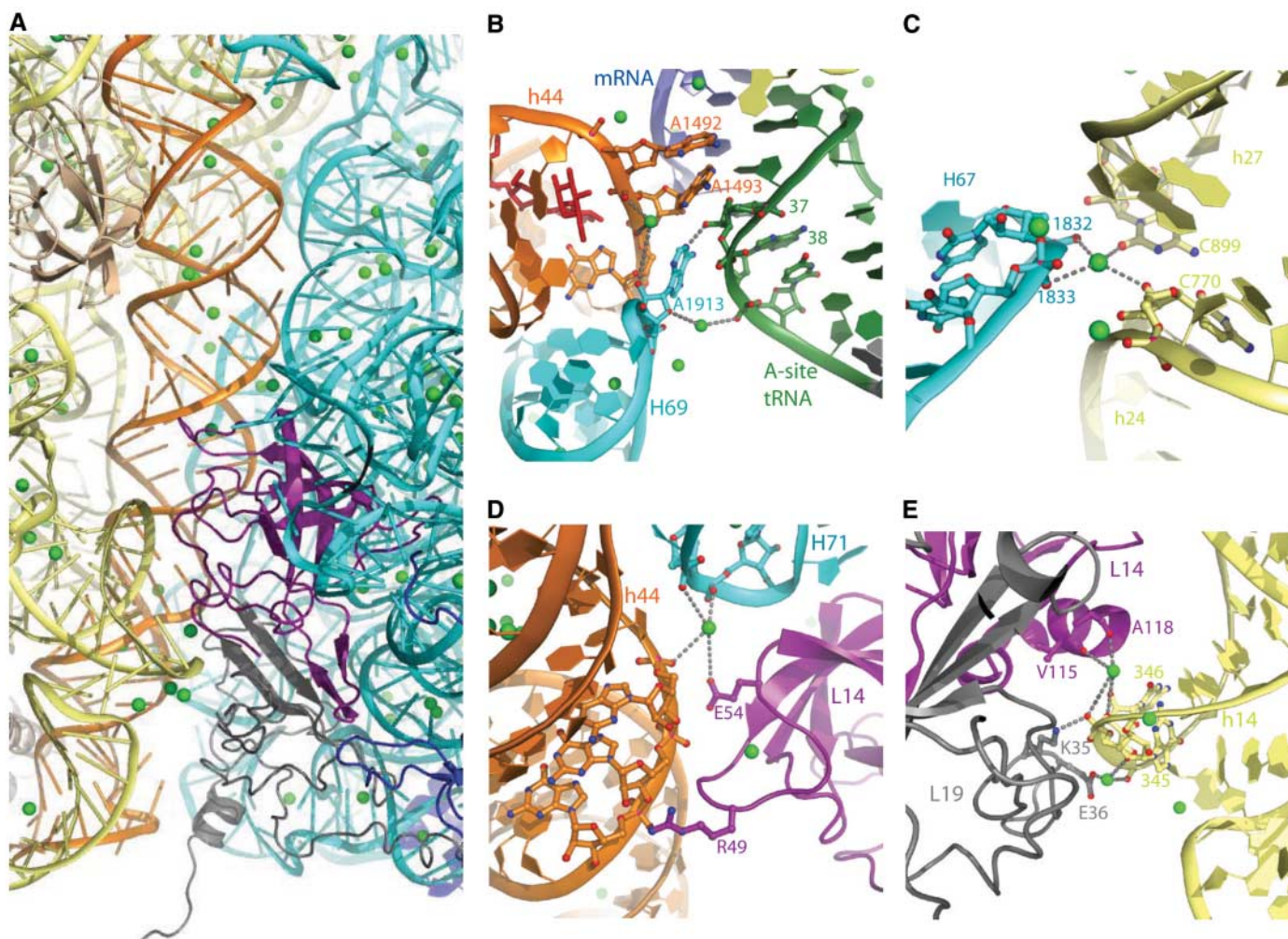


**Fig. 6.** Examples of the roles of metal ions and proteins in the intersubunit bridges. **(A)** Overview of the extensive intersubunit bridge interactions that 50S proteins L19 (gray) and L14 (purple) makes with h44 of 16S RNA (orange). L14 is involved in bridge B5 that interacts with 16S h44, L19 is involved with bridge B6 that interacts with 16S RNA h44, and both L14 and L19 are involved in bridge B8 that interacts with h14. The 23S RNA is shown in cyan, 50S proteins in blue, 16S RNA (except for h44) in yellow, 30S proteins in tan, and Mg ions in green. **(B)** An example of an induced change in a bridge on A-site tRNA binding. In bridge B2a, A1913 of H69 of 23S RNA flips out of its loop toward 16S RNA bases A1492 and A1493 to form a hydrogen bond with A37 of A-site tRNA. Two Mg ions (green) also interact with A1913: One is coordinated between its O4' and nonbridging phosphate oxygen of U38 of A-site tRNA, and another between its 2'-OH and the nonbridging phosphate oxygens of both 1492 and 1493. Paromomycin is shown in red and mRNA in purple. **(C)** A Mg-mediated bridge. In bridge B2c, a Mg ion (green) mediates the interaction between

the RNA backbones of h24 and h27 of 16S RNA and H67 of 23S RNA. The Mg ion is coordinated between the 2'-OH of 770 and O2 of C899 of 16S RNA and the nonbridging phosphate oxygens of 1832 and 1833 of 23S RNA. **(D and E)** Proteins and ions in bridges. In bridge B5 (D), L14 is involved by either directly interacting with the backbone of 16S RNA or via a Mg ion (green) that also contacts the backbone of both 16S and 23S RNA. Arg<sup>49</sup> of L14 interacts directly with the backbone of 1423 of 16S RNA, and Glu<sup>54</sup> is coordinated to a Mg ion that in turn interacts with the backbones of nucleotide 1421 of 16S RNA and 1950 and 1951 of 23S RNA. Bridge B8 (E) consists of interactions of the backbone of h14 of 16S RNA with both L14 and L19 via two Mg ions (green). In the center, a Mg ion is coordinated to the backbone oxygens of both Val<sup>115</sup> and Ala<sup>118</sup> of L14 and to h14 of 16S RNA. Below and to the left, a Mg ion is coordinated between the side chain of Lys<sup>35</sup> of L19 and h14 of 16S RNA. These interactions show the importance of Mg ions in additionally helping to stabilize bridging interactions between the 50S and 30S subunits.

## References and Notes

- N. Ban, P. Nissen, J. Hansen, P. B. Moore, T. A. Steitz, *Science* **289**, 905 (2000).
- B. T. Wimberly *et al.*, *Nature* **407**, 327 (2000).
- M. M. Yusupov *et al.*, *Science* **292**, 883 (2001); published online 29 March 2001 (10.1126/science.1060089).
- B. S. Schuwirth *et al.*, *Science* **310**, 827 (2005).
- K. Mitra, J. Frank, *Annu. Rev. Biophys. Biomol. Struct.* **35**, 299 (2006).
- A. Nikulin *et al.*, *Nat. Struct. Biol.* **10**, 104 (2003).
- M. Diaconu *et al.*, *Cell* **121**, 991 (2005).
- Materials and methods are available as supporting material on Science Online.
- L. Jenner *et al.*, *Science* **308**, 120 (2005).
- J. Harms *et al.*, *Cell* **107**, 679 (2001).
- J. M. Ogle, F. V. Murphy, M. J. Tarry, V. Ramakrishnan, *Cell* **111**, 721 (2002).
- D. Moazed, H. F. Noller, *Nature* **342**, 142 (1989).
- J. M. Ogle *et al.*, *Science* **292**, 897 (2001).
- U. L. RajBhandary, C. M. Chow, in *tRNA: Structure, Biosynthesis and Function*, D. Söll, U. L. RajBhandary, Eds. (American Society for Microbiology Press, Washington, DC, 1995), pp. 511–528.
- E. Schmitt, M. Panvert, S. Blanquet, Y. Mechulam, *EMBO J.* **17**, 6819 (1998).
- U. von Ahsen, H. F. Noller, *Science* **267**, 234 (1995).
- N. M. Abdi, K. Fredrick, *RNA* **11**, 1624 (2005).
- P. Nissen, J. A. Ippolito, N. Ban, P. B. Moore, T. A. Steitz, *Proc. Natl. Acad. Sci. U.S.A.* **98**, 4899 (2001).
- D. J. Battle, J. A. Doudna, *Proc. Natl. Acad. Sci. U.S.A.* **99**, 11676 (2002).
- L. Lancaster, H. F. Noller, *Mol. Cell* **20**, 623 (2005).
- J. Frank, R. K. Agrawal, *Nature* **406**, 318 (2000).
- A. P. Carter *et al.*, *Nature* **407**, 340 (2000).
- L. Jovine, S. Djordjevic, D. Rhodes, *J. Mol. Biol.* **301**, 401 (2000).
- H. Shi, P. B. Moore, *RNA* **6**, 1091 (2000).
- T. M. Schmeing *et al.*, *Nat. Struct. Biol.* **9**, 225 (2002).
- T. M. Schmeing, K. S. Huang, S. A. Strobel, T. A. Steitz, *Nature* **438**, 520 (2005).
- A. Bashan *et al.*, *Mol. Cell* **11**, 91 (2003).
- J. S. Weinger, K. M. Parnell, S. Dorner, R. Green, S. A. Strobel, *Nat. Struct. Mol. Biol.* **11**, 1101 (2004).
- M. D. Erlacher *et al.*, *Nucleic Acids Res.* **33**, 1618 (2005).
- S. V. Kirillov, J. Wower, S. S. Hixson, R. A. Zimmermann, *FEBS Lett.* **514**, 60 (2002).
- B. A. Maguire, A. D. Benjaminov, H. Ramu, A. S. Mankin, R. A. Zimmermann, *Mol. Cell* **20**, 427 (2005).
- H. Wang *et al.*, *Protein Sci.* **13**, 2806 (2004).
- U. Geigenmuller, K. H. Nierhaus, *EMBO J.* **9**, 4527 (1990).
- D. Moazed, H. F. Noller, *Cell* **57**, 585 (1989).
- Y. P. Semenov, M. V. Rodnina, W. Wintermeyer, *Proc. Natl. Acad. Sci. U.S.A.* **93**, 12183 (1996).
- R. Lill, J. M. Robertson, W. Wintermeyer, *EMBO J.* **8**, 3933 (1989).
- J. S. Feinberg, S. Joseph, *Proc. Natl. Acad. Sci. U.S.A.* **98**, 11120 (2001).
- T. M. Schmeing, P. B. Moore, T. A. Steitz, *RNA* **9**, 1345 (2003).
- G. Z. Yusupova, M. M. Yusupov, J. H. Cate, H. F. Noller, *Cell* **106**, 233 (2001).
- M. Osswald, B. Greuer, R. Brimacombe, *Nucleic Acids Res.* **18**, 6755 (1990).
- J. W. Kenny, R. R. Traut, *J. Mol. Biol.* **127**, 243 (1979).
- A. J. Eistetter, P. D. Butler, R. R. Traut, T. G. Fanning, *FEMS Microbiol. Lett.* **180**, 345 (1999).
- T. Hard, A. Rak, P. Allard, L. Kloos, M. Garber, *J. Mol. Biol.* **296**, 169 (2000).
- F. C. Chao, *Arch. Biochem. Biophys.* **70**, 426 (1957).
- J. Frank *et al.*, *Biochem. Cell Biol.* **73**, 757 (1995).
- S. Ghosh, S. Joseph, *RNA* **11**, 657 (2005).
- W. L. DeLano, <http://pymol.sourceforge.net/> (2006).
- Crystals were screened at Daresbury Labs, UK, or at European Synchrotron Radiation Facility (ESRF), Grenoble, France. Data were collected at the Swiss Light Source, Paul Scherrer Institut, Villigen, Switzerland, and at ESRF. We thank C. Schulze-Briese and R. Ravelli for help and advice with data collection; W. Kabsch for advice with the data integration program XDS; P. Adams for advice and for modifying the refinement program CNS; D. Gohara for optimally compiling an operating system X version of this modified CNS; P. Emsley for advice with the graphics program COOT; K. Nierhaus and E. Schmitt for gifts of overproducing clones of Phe- and fMet-tRNAs, respectively; and T. M. Schmeing for critical comments. This work was supported by the Medical Research Council (UK), NIH grant GM67624, the Agouron Institute and fellowships from the Wenner-Gren Foundations (M.S.), the American Cancer Society (C.M.D.), European Molecular Biology Organization (E.V.M.), Austrian Academy of Sciences (A.W.), and the Boehringer-Ingelheim Fond (S.P.). Coordinates and structure factors have been deposited with the Protein Data Bank (PDB) with accession codes 2j00 (30S-1), 2j01 (50S-1), 2j02 (30S-2), and 2j03 (50S-2). V.R. holds stock options in and is on the Scientific Advisory Board of Rib-X Pharmaceuticals, a company that develops antibacterial drugs that target the ribosome.

## Supporting Online Material

[www.sciencemag.org/cgi/content/full/1131127/DC1](http://www.sciencemag.org/cgi/content/full/1131127/DC1)

Materials and Methods

Figs. S1 to S5

Tables S1 to S4

References

12 June 2006; accepted 9 August 2006

Published online 7 September 2006;

10.1126/science.1131127

Include this information when citing this paper.

## REPORTS

# Tunable Quasi-Two-Dimensional Electron Gases in Oxide Heterostructures

S. Thiel,<sup>1</sup> G. Hammerl,<sup>1</sup> A. Schmehl,<sup>2</sup> C. W. Schneider,<sup>1</sup> J. Mannhart<sup>1\*</sup>

We report on a large electric-field response of quasi-two-dimensional electron gases generated at interfaces in epitaxial heterostructures grown from insulating oxides. These device structures are characterized by doping layers that are spatially separated from high-mobility quasi-two-dimensional electron gases and therefore present an oxide analog to semiconducting high-electron mobility transistors. By applying a gate voltage, the conductivity of the electron gases can be modulated through a quantum phase transition from an insulating to a metallic state.

Complex oxides show a broad spectrum of intrinsic functionalities, such as ferroelectricity, magnetism, superconductivity, and multiferroic behavior [see (1)], which can be used and combined in electronic devices

that are based on epitaxially grown heterostructures. Physical properties may arise in such multilayers that are not found in either of their constituents. One example, a conducting quasi-two-dimensional electron gas (q2-DEG) is formed at the interface between the two insulating, dielectric perovskites, LaAlO<sub>3</sub> and SrTiO<sub>3</sub> (2, 3). The electrons at this interface are highly mobile, with values up to 10<sup>4</sup> cm<sup>2</sup> V<sup>-1</sup> s<sup>-1</sup> (4, 2 K) having been reported (2–5), and were found to have densities orders of magnitude higher than the densities of two-dimensional electron gases

induced at interfaces in heterostructures based on III-V semiconductors. Exploring whether the q2-DEGs can be applied to fabricate high electron mobility transistor (HEMT)-type field effect devices (6), we observed that they can be tuned by altering on the unit cell level the thickness of the LaAlO<sub>3</sub> sheets. For LaAlO<sub>3</sub> layers that are up to 3 unit cells (uc) thick, highly insulating interfaces are obtained. In field-effect transistor configurations that use such interfaces as drain-source (DS) channels, a phase transition to the conducting state is readily achieved by gate fields. Upon change of their carrier densities with applied electric fields, the q2-DEGs react with a pronounced memory effect.

Previous work revealed the existence of metallic electron gases at LaTiO<sub>3</sub>-SrTiO<sub>3</sub> (7) and at LaAlO<sub>3</sub>-SrTiO<sub>3</sub> interfaces (2, 3). Because electron energy loss measurements of LaTiO<sub>3</sub>-SrTiO<sub>3</sub> interfaces showed that the electron gas is confined within a ~2-nm-thick layer (7), the gas is described to be quasi-two dimensional. Whereas the LaTiO<sub>3</sub>-SrTiO<sub>3</sub> interface is doped by transfer of electrons from the LaTiO<sub>3</sub> to the SrTiO<sub>3</sub> (7, 8), for the LaAlO<sub>3</sub>-SrTiO<sub>3</sub> interface two different mechanisms have been reported to generate the gas: In some heterostructures, it was found (2, 3) that the carriers are induced by the polarity discontinuity of the TiO<sub>2</sub>-LaO<sup>+</sup> stacking

<sup>1</sup>Experimental Physics VI, Center for Electronic Correlations and Magnetism, Institute of Physics, University of Augsburg, D-86135 Augsburg, Germany. <sup>2</sup>Department of Materials Science and Engineering, Pennsylvania State University, University Park, PA 16802-5005, USA.

\*To whom correspondence should be addressed. E-mail: jochen.mannhart@physik.uni-augsburg.de

## Supporting Online Material for

Maria Selmer,<sup>\*</sup> Christine M. Dunham<sup>\*</sup>, Frank V. Murphy, IV,  
Albert Weixlbaumer, Sabine Petry, Ann C. Kelley,  
John R. Weir, and V. Ramakrishnan<sup>†</sup>

<sup>\*</sup> These authors contributed equally to this work.

<sup>†</sup>To whom correspondence should be addressed.

Email: ramak@mrc-lmb.cam.ac.uk

### **This PDF files includes:**

Materials and Methods

Tables S1-S4

Figures S1-S5

References

## Materials and methods

### **Ribosomes**

*Thermus thermophilus* 70S ribosomes were isolated as described (1, 2). All buffers contained 6 mM 2-mercaptoethanol, 0.1 mM benzamidine and 0.5 mM phenyl-methyl-sulfonyl fluoride added just before use. All procedures were done at 0-4 °C. Briefly, frozen cell paste of *Thermus* cells was resuspended in 1.5 ml of buffer A (100 mM NH<sub>4</sub>Cl, 10.5 mM Mg-acetate, 0.5 mM EDTA, 20 mM K-Hepes, pH 7.5) per gram of cell paste. After the addition of DNase I (8 µg per g of cell paste), the cells were disrupted in an Emulsiflex cell disruptor. The disrupted cell slurry was then centrifuged at 30,000 rpm in a Beckman 45Ti rotor for 1 hour. The supernatant was carefully removed, taking care not to disturb the pellet consisting of cell debris, and then layered over a sucrose cushion of at least 25 ml of buffer B (1.1 M sucrose, 0.5 M KCl, 10.5 mM Mg-acetate, 0.5 mM EDTA, 20 mM Hepes, pH 7.5) in a 45Ti centrifuge tube, and centrifuged at 45,000 rpm in a 45 Ti rotor for 17.5 hours. The ribosomal pellet was washed lightly in buffer C (1.5 M ammonium sulfate, 10 mM Mg-acetate, 400 mM KCl, 20 mM Tris-Cl, pH 7.5) to remove any “skin” of cell debris, resuspended in the same buffer and then applied to a Toyopearl butyl 650S column equilibrated in the same buffer. The 70S peak was eluted by a reverse gradient of ammonium sulfate, keeping the other components of buffer C constant.

The ribosomal peak, which should now be free of a contaminating endogenous ribonuclease, was diluted 2-fold in buffer E (50 mM KCl, 10 mM NH<sub>4</sub>Cl, 10.25 mM Mg-acetate, 0.25 mM EDTA, 10 mM HEPES, pH 7.5), pelleted overnight by centrifugation at 43,000 rpm in a 45Ti rotor, and resuspended in buffer E. The 70S ribosomes were then separated from excess 50S or 30S subunits by zonal ultracentrifugation a Ti15 zonal rotor with a gradient of 10 – 40% sucrose in buffer E. The 70S ribosomes were diluted in buffer E without sucrose, and pelleted as above. They were resuspended in buffer G (50 mM KCl, 10 mM NH<sub>4</sub>Cl, 10 mM Mg-acetate, 5 mM HEPES, pH 7.5) at a concentration of approximately 350 A260 units/ml, and stored in aliquots at -80 C until use for complex formation.

### **mRNA and tRNAs**

The mRNA and ASL oligonucleotides were chemically synthesized (Dharmacon). The sequence of mRNA Z4C was modified from that of Yusupova *et al.* (3): 5'GGCAAGGAGGUAAAAAUGUUCAAA-3' (the codons for fMet and Phe are underlined). The tRNAs were overexpressed, purified and charged as previously described for tRNA<sup>Phe</sup> (4) and tRNA<sup>fMet</sup> (5).

### **Complex formation**

All complexes were formed in buffer G (5 mM HEPES pH 7.5, 10 mM MgAc, 50 mM KCl, 10 mM NH<sub>4</sub>Cl, 6 mM 2-mercaptoethanol). To form a pre-translocational complex,

4.4  $\mu\text{M}$  70S ribosomes were programmed with 8.8  $\mu\text{M}$  mRNA Z4C and incubated at 55°C for 5 min, after which 17.6  $\mu\text{M}$  tRNA<sup>Met</sup> was added and the complex incubated at 55°C for 30 min. At this point, 17.6  $\mu\text{M}$  Phe-tRNA<sup>Phe</sup> was added and the complex incubated at 55°C for 30 min. After addition of 0.1 mM paromomycin, the complex was left at room temperature for 30 min prior to crystallization.

### **Crystallization**

Crystallization conditions were screened using 100 nl drops (6). Initial crystalline needles were observed using the Clear Strategy Screen (Molecular Dimensions) in 0.2M KSCN, 8% PEG 20K, 8% PEG550 MME, 0.1M TRIS-HAc pH 8.5. Crystals were grown in sitting drop vapor diffusion experiments in which 2.4-3.6  $\mu\text{l}$  of ribosomal complex including 2.8 mM Deoxy Big Chap (Hampton Research) was mixed with 2-3  $\mu\text{l}$  reservoir solution containing 0.2M KSCN, 0.1M Tris-HAc pH7, 3.5-4.5% (w/v) PEG20K, 3.5-4.5% (w/v) PEG550MME and left to equilibrate at 20°C. Crystals grew in 4-14 days to the size of up to 50x70x700  $\mu\text{m}$ . The crystals were sequentially transferred to cryo-protecting solution (0.2M KSCN, 0.1M Tris-HAc pH 7, 5% PEG 20K, 25% PEG550MME), and frozen by plunging into liquid nitrogen. All data collection was carried out at 100K.

### **Data collection, refinement and model building**

Crystals were pre-screened at the beamlines 14.1 at SRS, Daresbury Laboratory and 14-1 and 14-2 at ESRF, Grenoble. An initial data set to 4.6 Å resolution was collected at beamline 14-4 at ESRF, Grenoble. X-ray diffraction data were measured at beamline X10SA at the Swiss Light Source, Villigen. To obtain the maximum possible redundancy and signal-to-noise, three complete data sets were collected from separate regions of the same crystal, while keeping exposure to a minimum on each pass. Data were integrated and scaled with the XDS package (7). The crystals belong to spacegroup P2<sub>1</sub>2<sub>1</sub>2<sub>1</sub> with cell dimensions of  $a=214$  Å,  $b=454$  Å,  $c=630$  Å,  $\alpha = \beta = \gamma = 90^\circ$ .

The structure was solved by molecular replacement with CNS (8) using the all-atom model of the *Thermus* 70S ribosome at 5.5 Å resolution (9) for the initial search. The tRNA and mRNA ligands were not included in the search model. Molecular replacement produced two clear solutions showing the presence of two molecules in the asymmetric unit. The initial solution was refined by rigid body refinement followed by energy minimization and group B-factor refinement in CNS. Refinement after each round of model building was carried out as follows: First, energy minimization and group B-factor refinement was carried out from 6.0-2.8 Å without bulk solvent correction. The resulting refined model was used to optimize bulk solvent parameters in a grid search, using a grid of 0.25 for the mask calculation. The structure was then refined from 50-2.8 Å including bulk solvent correction, using simulated annealing and a second round of grouped B-factor refinement. Non-crystallographic restraints were applied separately to the 4 major domains of the 30S ribosomal subunit (body, platform, head and 3' minor domain), the L1 stalk, L7/L12 stalk and the rest of the 50S subunit. Parallel refinement done without NCS restraints did not show major differences.

Rebuilding of the RNA was done after minor correction of the sequence to reflect that from the *Thermus thermophilus* HB8 genome sequence. Both the low resolution structure of the *Thermus* ribosome and the high-resolution *E. coli* ribosome structure (9, 10) were very useful guides for the rebuilding of 23S RNA, while the high resolution structure of the 30S ribosomal subunit (11) was likewise useful to build 16S RNA.

The 30S proteins were rebuilt using the high-resolution structure of the subunit (11). For the 50S proteins, a homology model was constructed using Swiss-Model (12), starting with either structures solved in isolation (preferably from *Thermus* when available), or those in the *Deinococcus* 50S subunit (13) or 70S ribosome (10). This homology model was used as a starting point to build the protein structures into density. For some proteins such as L28 and L31, or additional domains of proteins, structures had to be built from scratch. Model building was done mainly in COOT(14). Many of the 50S proteins were rebuilt using O (15) to take advantage of its library of structures to impose good geometry.

**Table S1. Data collection and refinement statistics**

<b>Data Collection</b>	
Space Group	P2 <sub>1</sub> 2 <sub>1</sub> 2 <sub>1</sub>
Cell dimensions	213.3 x 453.0 x 631.4 (Å)
Resolution (Å) <sup>1</sup>	50 – 2.8 (2.9-2.8)
<i>I</i> / $\sigma$ ( <i>I</i> )	7.3 (2.1)
<i>R</i> <sub>sym</sub> (%)	28.1 (75.0) <sup>2</sup>
No. of unique reflections	1382065
Completeness (%)	91.8 (72.4) <sup>2</sup>
Redundancy	9.1 (4.6)
<b>Refinement<sup>3</sup></b>	
Resolution	50 – 2.8 (2.9-2.8)
<i>R</i> <sub>work</sub> / <i>R</i> <sub>free</sub> (%)	27.8/31.7 (36.7/39.1) <sup>4</sup>
No. of atoms	
RNA	98760 (per molecule)
Protein	46434
Ions	491(molecule I)+560 (molecule II)
RMS deviations	
Bond lengths	0.0087
Bond angles	1.27

1. Parenthesis indicate outer shell for later statistics
2. The higher than normal *R*<sub>sym</sub> is at least partly due to the large redundancy in observations, combined with low signal-to-noise in individual measurements. However, unbiased difference Fourier maps show more detail than typical 3-3.2 Å maps of the 30S subunit (see Fig. 1 of main paper). For the 3.2 – 3.1 Å shell, the completeness was 99.1%, *R*<sub>sym</sub> was 70.3% and *I*/ $\sigma$ (*I*) was 3.0
3. Refinement was carried out with NCS restraints as described in the Materials and Methods above.
4. For the free R-factor, 5% of the reflections were used. *R*<sub>work</sub>/*R*<sub>free</sub> = 0.35/0.38 at 3.2-3.1 Å. The *R*<sub>work</sub>/*R*<sub>free</sub> are typical of structures of this size.

## Table S2. Comparison of 16S and 23S RNA from other 70S ribosome structures

*Root-mean-squared deviation and median (Angstroms) of equivalent phosphorus atoms*

RNA	Rmsd (Å)	Median (Å)
<b>16S</b>		
1GIX	3.06	2.22
1YL4	1.82	1.24
1AVY	3.92	1.78
1AW7	7.03	1.76
<b>23S</b>		
1GIY	4.15	2.35
1YL3	2.97	0.88
1AW4	2.86	0.96
1AWB	2.56	0.94

1GIX and 1GIY from ref .(16)

1YL4 and 1YL3 from ref . (9)

1AVY, 1AW7 and 1AW4, 1AWB from ref. (10)

**Table S3: Summary of rebuilt proteins**

Protein	Number of residues (with N-terminal M)	Visible residues	structure of isolated protein known	Reference	comment
L1	228	K18-H27, V43-L75, A119-A146, A158-A224	<i>S. acidocalarius</i> 2.65Å crystal structure of L1 and 55nt 23S rRNA (PDB ID: 1MZP)	(17)	Poly Ala for 119-146 and 158-224
L2	276	A2-R274	RNA binding domain (60-195) of <i>B. stearrowthermophilus</i> at 2.3Å (PDB ID: 1RL2)	(18)	
L3	206	M1 - A204	-		modeled on <i>H.ma.</i> 50S and <i>E. coli</i> 70S/ <i>D. rad.</i> 50S; extensive rebuilding required
L4	210	M1 - G207	<i>T. maritima</i> at 1.7 Å (loop region extending in ribosome missing, PDB ID: 1DMG)	(19)	N-terminus reported as disordered in <i>E. coli</i> is forming a helix
L5	182	L3-K182	<i>B. stearrowthermophilus</i> at 1.8Å (PDB ID: 1IQ4)	(20)	
L6	177	P8-R170	<i>B. stearrowthermophilus</i> at 2Å (PDB ID: 1RL6)	(21)	C-terminal domain deviates from crystal structure
L7/L12	125	none	part of <i>T.maritima</i> L7/L12 Stalk structure at up to 1.9 Å (PDB ID: 1ZAV, 1ZAW, 1ZAX)	(22)	L7/L12 stalk disordered
L9	148	M1-V145	<i>B. stearrowthermophilus</i> at 2.6Å (PDB ID: 1DIV)	(23)	
L10	173	none	part of <i>T.maritima</i> L7/L12 Stalk structure at up to 1.9 Å (PDB ID: 1ZAV, 1ZAW, 1ZAX)	(22)	
L11	147	none	<i>T. maritima</i> L11 bound to 23S rRNA fragment at 2.8Å (PDB ID: 1MMS)	(24)	whole L11 RNA binding region disordered

Protein	Number of residues (with N-terminal M)	Visible residues	structure of isolated protein known	Reference	comment
L13	140	M1- V140	<i>P. horikoshii</i> at 1.6Å (PDB ID: 1J3A)	not published	<i>T. thermophilus</i> protein contains an additional N-terminal tail (1-13) and two extra loops (36-49 and 73-88)
L14	122	M1-L122	<i>B. stearrowthermophilus</i> at 1.5Å (PDB ID: 1WHI)	(25)	
L15	150	A12 – A150	-		modeled on <i>H.ma.</i> 50S and <i>E. coli</i> 70S/ <i>D. rad.</i> 50S; extensive rebuilding required, C-terminal domain completely built in contrast to previous structures
L16	141	R6 – Q141	<i>T. thermophilus</i> NMR structure (PDB ID: 1WKI)	(26)	
L17	118	R2-E118			
L18	112	E8-E103	<i>T. thermophilus</i> NMR structure (PDB ID: 1ILY)	(27)	
L19	146	M1-K137	-		modeled on <i>E. coli</i> 70S/ <i>D. rad.</i> 50S; extensive rebuilding required
L20	118	P2 – G118			same as above
L21	101	M1 – G101	-		same as above
L22	113	M1-K113	-		
L23	96	T3-G94	<i>T. thermophilus</i> NMR structure (PDB ID: 1N88)	(28)	
L24	110	R2-K101	-		extensive building, modeled on <i>D. rad.</i> and <i>H. ma.</i> 50S/ <i>E. coli</i> 70S

Protein	Number of residues (with N-terminal M)	Visible residues	structure of isolated protein known	Reference	comment
L25	206	Y3 – V174	<i>T. thermophilus</i> at 2.3Å in complex with a fragment of 5S rRNA (PDB ID: 1FEU)	(29)	N-terminal domain interacting with 5S rRNA very similar, C-terminal domain with conformational changes
L27	85	1-9 Poly-Ala T10-A85	<i>T. thermophilus</i> at 2.8Å (PDB ID: 1V8Q)	(30)	incorrect fold in previous ribosome structures
L28	98	S8 – L95	-		was previously misinterpreted as L31; L28 built from scratch with additional helix
L29			<i>T. maritima</i> NMR structure (PDB ID: 1R73)	(31)	
L30	60	M1-V59	<i>T. thermophilus</i> at 1.9Å (PDB ID 1BXY)	(32)	
L31	71	49	-		all Poly Ala
L32	60	A2 - V60	-		modeled on <i>D. rad.</i> 50S/ <i>E. coli</i> 70S as basis
L33	54	L9-V52	-		
L34	49	M1-K48	-		same as above
L35	65	P2-Y64	-		same as above
L36	37	none	<i>T. thermophilus</i> NMR structure (PDB ID: 1DFE and 1DGZ)	(33)	no density visible at reported binding site
S2	256	V7-Q240	-		correction of registry necessary
S13	126	E8-R125	-		

**Table S4. Proteins and ions in inter-subunit bridges*****Interactions of inter-subunit bridging ions***

<b>Bridge</b>	<b>30S</b>	<b>50S</b>
B2c (Mg-mediated only)	h24: C770 OP h24: C770 2'OH, h27: C899 O2, h24:G771 OP h27: A900 2'OH	H67: U1833 OP, base of H57: C1468 OP H67: C1832 OP, U1833 OP H67: C1832 2'OH, U1833 OP
B4	S15 Arg 88 O, S15 89 Gly O	H34: A716 OP, U714 OP
B5	h44: G1421 OP h44: G1475 OP (4.85)	L14 Glu 54 O, H77: 1950 OP, 1951 OP H64: C1767, H62: A1689 2'OH
B6 (water molecule)	h44: C1430 O4', C1429 2'OH	H62: G1703 2'OH, G1704 OP,
B8	h14: G345 OP, G346 OP h14: G347 OP	L19 Glu 36 OE1, OE2 L14 Val 115 O, Ser 116 O, Ala 118 O

***Protein interactions in inter-subunit bridges\****

<b>Bridge</b>	<b>30S</b>	<b>50S</b>
B4	S15 Leu 56, Val 60 S15 His 53 NE2 S15 Arg 64 NH2	23S G715 (hydrophobic interaction) 23S G715 O6 23S G715 OP
B5	16S G1423 OP, G1422 O3'	L14 Arg 49 NH1
B6	16S G1432 OP 16S C1463 OP	L19 Arg 108 NH1, NH2 L19 Arg 111 NE
B8	16S A338 OP 16S C339 OP 16S G346 OP	L14 Arg 97 NH2 L14 Arg 97 NH1 L19 Lys 35 NZ
New	16S A1442a N7	L19 Arg 118 NH1
New	S19 42, 65-67	L31

\* Only residues at 3.2 Å distance or closer

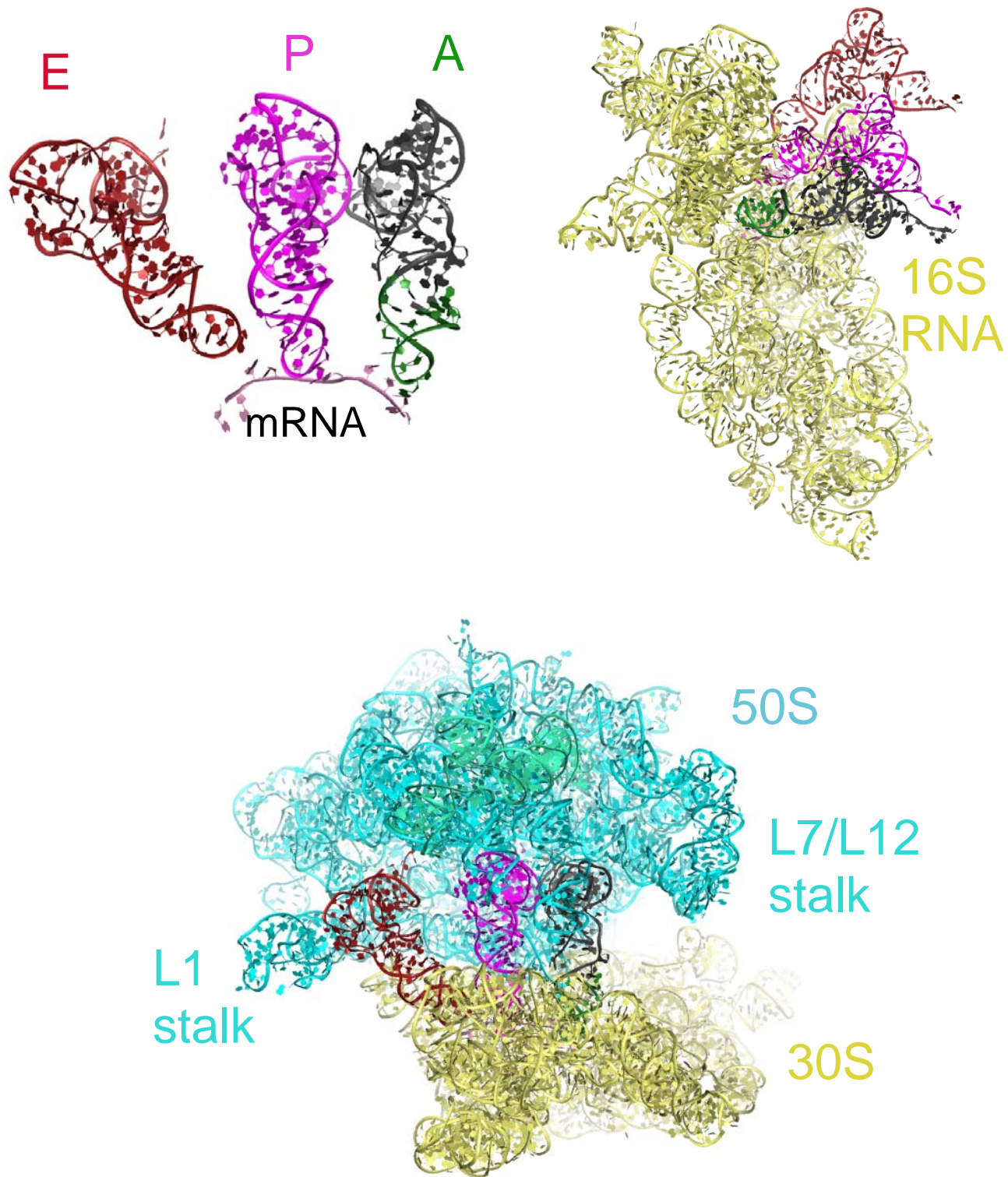


Fig. S1. Overview of the 70S structure. Top left: Orientation of the A, P and E site tRNAs and mRNA. Top right: Relative orientation of the tRNAs with respect to 16S RNA in the 30S subunit. Bottom: Relative orientation of tRNAs with respect to 23S and 5S RNA in the 50S subunit and 16S RNA in the 30S subunit. Ribosomal proteins are not shown.

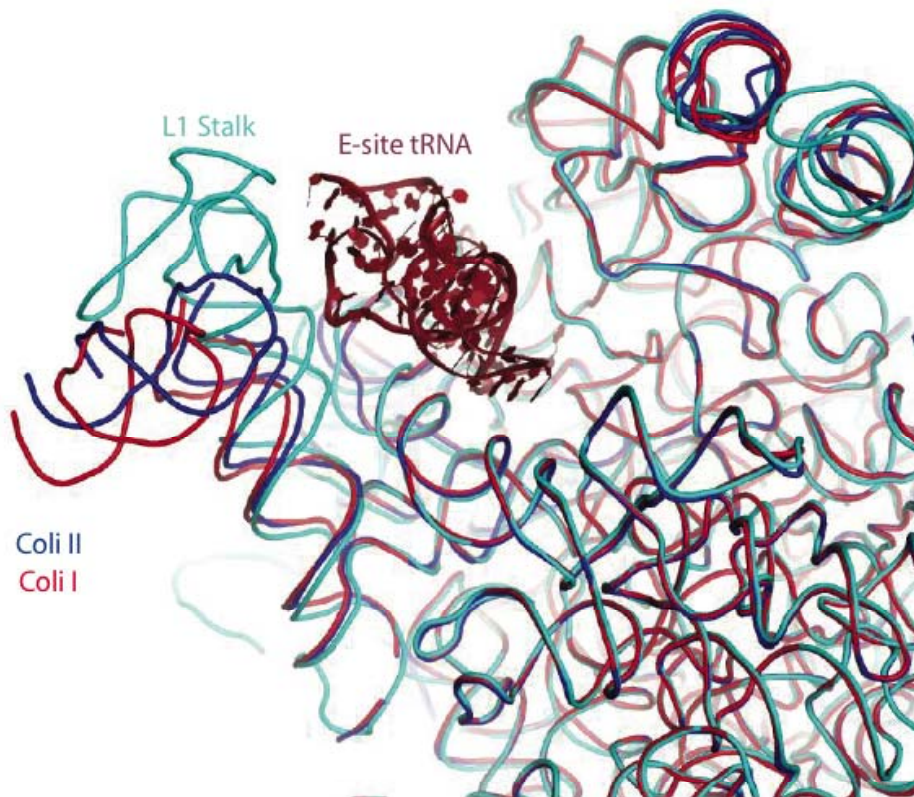


Fig. S2. Differences in the orientation of the L1 stalk between the *Thermus* 70S structure containing E site tRNA and the two molecules in the empty *E. coli* 70S structure (10).

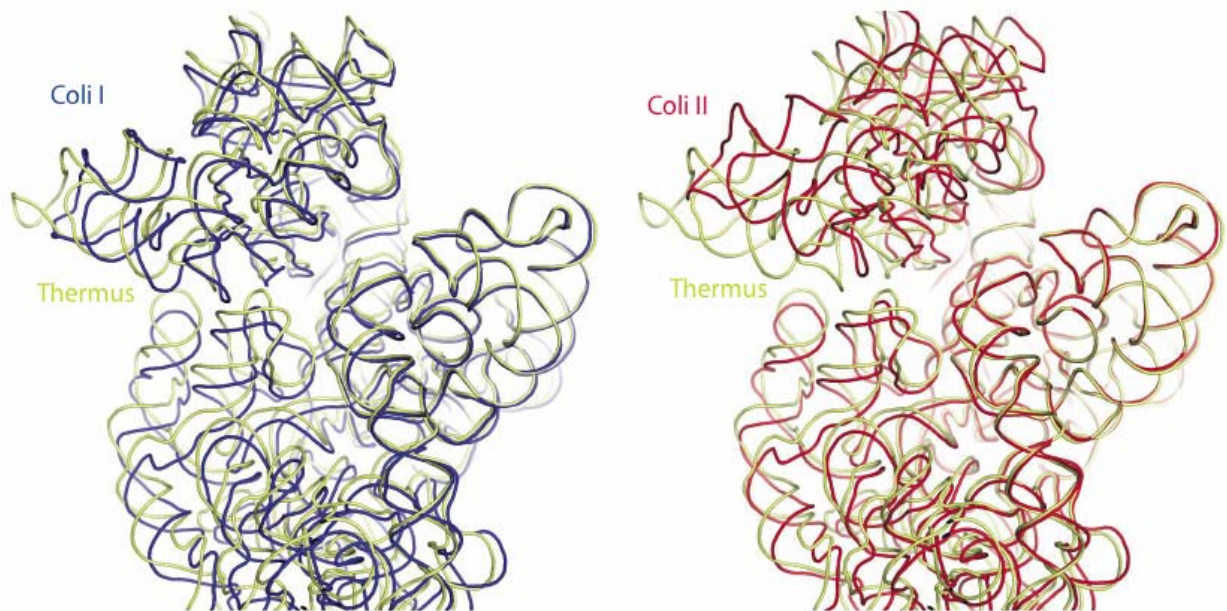


Fig. S3. Differences in the conformation of two empty *E. coli* 30S structures (10), compared to the *Thermus* structure containing mRNA and cognate A and P site tRNAs. If we align the 50S in the two *E. coli* 70S molecules with ours, the platforms of the 30S in molecule I is in a similar orientation, but the *E. coli* head and shoulder are slightly rotated towards the L1 stalk side. However, the 30S of molecule II is significantly more “open” than that of molecule I, with the head and shoulder moving apart from each other, and a significant rotation of the head towards the platform.

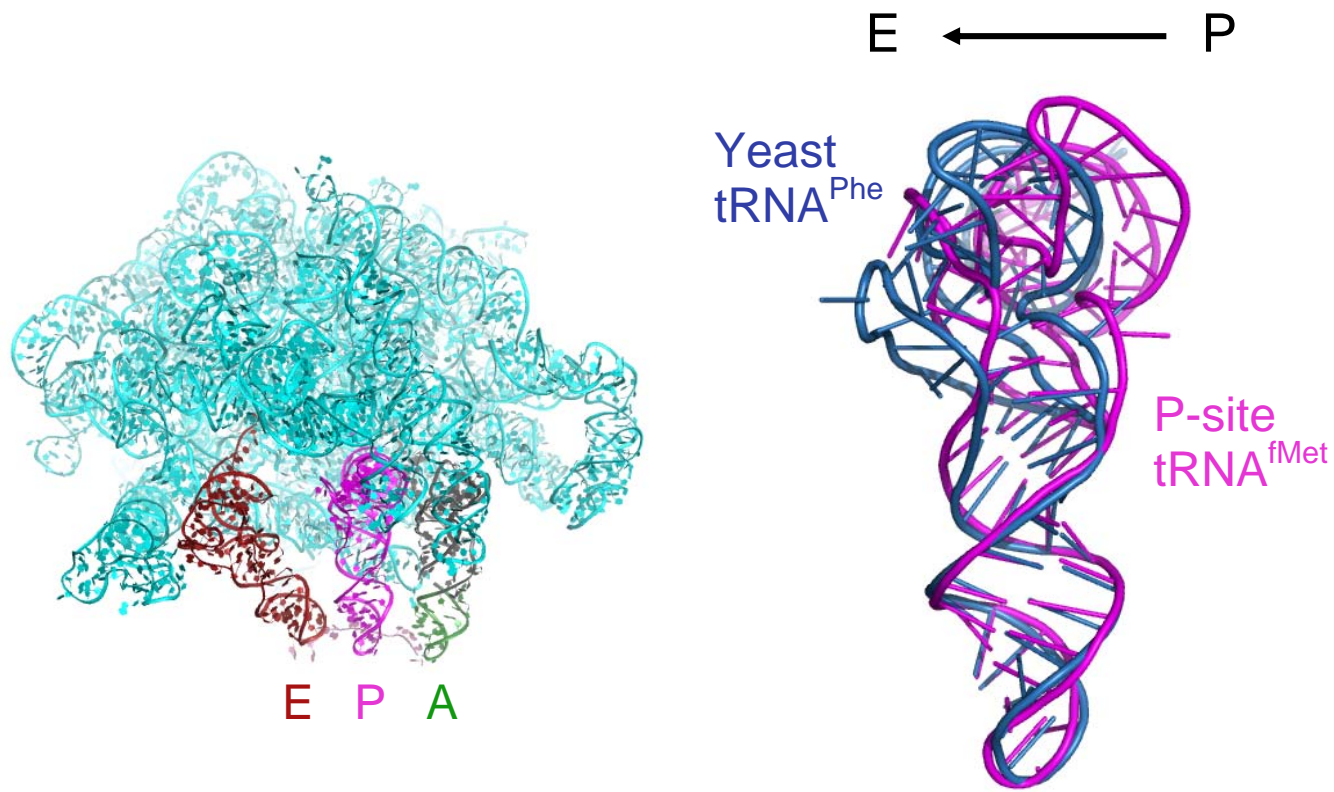


Fig. S4. Distortion of the P-site tRNA<sup>fMet</sup> relative to the crystal structure of isolated yeast tRNA<sup>Phe</sup> (34). Removal of constraints in the 50S would allow the tRNA to relax from its distorted form by moving towards the E site.

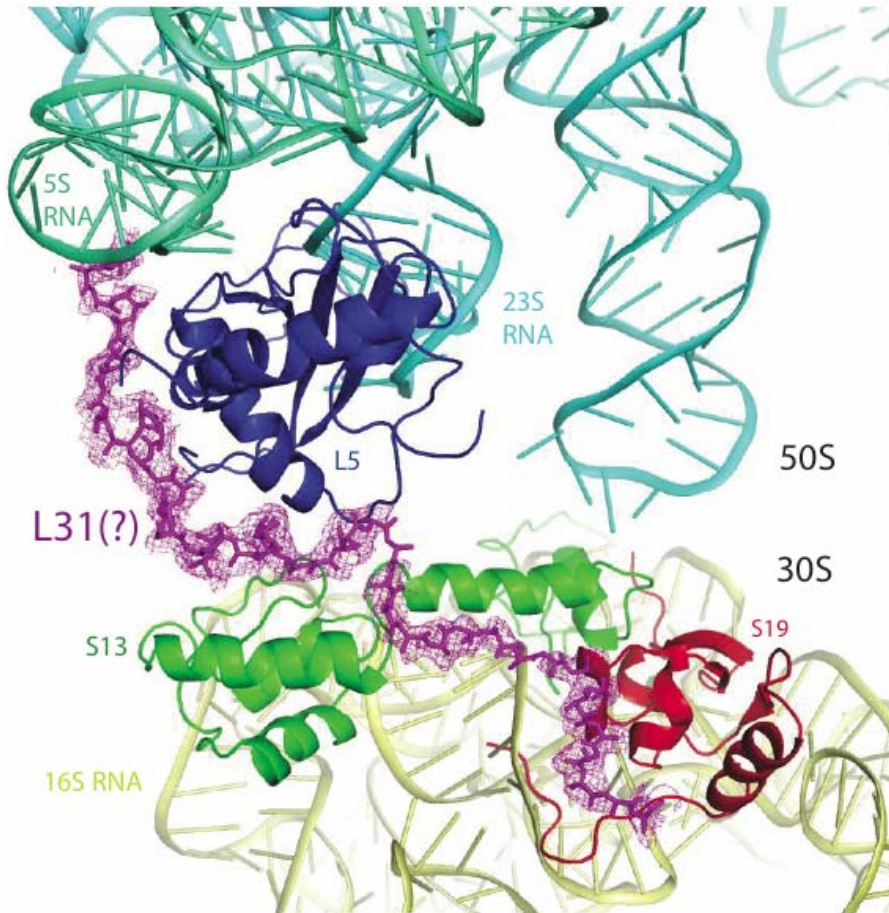


Fig. S5. Putative identification of L31 in the 50S structure. The protein makes contacts with L5, with which it is known to crosslink. It is also known to be tenuously associated with the ribosome. Both of these could be rationalized by this location (see text for details).

## References

1. W. M. Clemons, Jr. *et al.*, *J. Mol. Biol.* **310**, 827 (2001).
2. S. Petry *et al.*, *Cell* **123**, 1255 (2005).
3. G. Z. Yusupova, M. M. Yusupov, J. H. Cate, H. F. Noller, *Cell* **106**, 233 (2001).
4. R. Jünemann *et al.*, *Nucleic Acids Res.* **24**, 907 (1996).
5. E. Schmitt, M. Panvert, S. Blanquet, Y. Mechulam, *EMBO J.* **17**, 6819 (1998).
6. D. Stock, O. Perisic, J. Lowe, *Prog. Biophys. Mol. Biol.* **88**, 311 (2005).
7. W. Kabsch, *J. Appl. Cryst.* **26**, 795 (1993).
8. A. T. Brünger *et al.*, *Acta Crystallogr. D Biol. Crystallogr.* **54**, 905 (1998).
9. L. Jenner *et al.*, *Science* **308**, 120 (2005).
10. B. S. Schuwirth *et al.*, *Science* **310**, 827 (2005).
11. B. T. Wimberly *et al.*, *Nature* **407**, 327 (2000).
12. T. Schwede, J. Kopp, N. Guex, M. C. Peitsch, *Nucleic Acids Res.* **31**, 3381 (2003).
13. J. Harms *et al.*, *Cell* **107**, 679 (2001).
14. P. Emsley, K. Cowtan, *Acta Crystallogr. D Biol. Crystallogr.* **60**, 2126 (2004).
15. T. A. Jones, M. Kjeldgaard, *Methods Enzymol.* **277**, 173 (1997).
16. M. M. Yusupov *et al.*, *Science* **292**, 883 (2001).
17. A. Nikulin *et al.*, **10**, 104 (2003).
18. A. Nakagawa *et al.*, *EMBO J* **18**, 1459 (1999).
19. M. Worbs, R. Huber, M. C. Wahl, *EMBO J.* **19**, 807 (2000).
20. T. Nakashima *et al.*, *RNA* **7**, 692 (2001).
21. B. L. Golden, V. Ramakrishnan, S. W. White, *EMBO J.* **12**, 4901 (1993).
22. M. Diaconu *et al.*, *Cell* **121**, 991 (2005).
23. D. W. Hoffman *et al.*, *EMBO J.* **13**, 205 (1994).
24. B. T. Wimberly, R. Guymon, J. P. McCutcheon, S. W. White, V. Ramakrishnan, *Cell* **97**, 491 (1999).
25. C. Davies, S. W. White, V. Ramakrishnan, *Structure* **4**, 55 (1996).
26. M. Nishimura *et al.*, *J. Mol. Biol.* **344**, 1369 (2004).
27. E. A. Woestenenk *et al.*, *Biochem. J.* **363**, 553 (2002).
28. A. Ohman, A. Rak, M. Dontsova, M. B. Garber, T. Hard, *J. Biomol. NMR* **26**, 131 (2003).
29. R. Fedorov *et al.*, *Acta Crystallogr D Biol Crystallogr* **57**, 968 (2001).
30. H. Wang *et al.*, *Protein Sci.* **13**, 2806 (2004).
31. W. Peti *et al.*, *J Struct Funct Genomics* **5**, 205 (2004).
32. R. Fedorov *et al.*, *Acta Crystallogr. D Biol. Crystallogr.* **55**, 1827 (1999).
33. T. Hard, A. Rak, P. Allard, L. Kloo, M. Garber, *J. Mol. Biol.* **296**, 169 (2000).
34. H. Shi, P. B. Moore, *RNA* **6**, 1091 (2000).